



Cite this: *Nanoscale*, 2015, 7, 5262

## Dynamic control of the location of nanoparticles in hybrid co-assemblies†

Zhilong Su,<sup>a</sup> Xiaokang Li,<sup>b</sup> Xuesong Jiang,<sup>\*a</sup> Shaoliang Lin<sup>\*b</sup> and Jie Yin<sup>a</sup>

We herein demonstrated an approach to control the spatial distribution of components in hybrid microspheres. Hybrid core-shell structured microspheres (CSMs) prepared through co-assembly were used as starting materials, which are comprised of anthracene-ended hyperbranched poly(ether amine) (AN-hPEA) in the shell and crystallized anthracene containing polyhedral oligomer silsesquioxane (AN-POSS). Upon thermal annealing at a temperature higher than the melting point of AN-POSS, the diffusion of AN-POSS from the core to the shell of CSM leads to a transition of morphology from the core-shell structure to core-transition-shell to the more stable homogeneous morphology, which has been revealed by experimental results of TEM and DSC. The mechanism for the morphology transition of CSM induced by the diffusion of AN-POSS was disclosed by a dissipative particle dynamics (DPD) simulation. A mathematical model for the diffusion of POSS in the hybrid microsphere is established according to Fick's law of diffusion and can be used to quantify its distribution in CSM. Thus, the spatial distribution of POSS in the microsphere can be controlled dynamically by tuning the temperature and time of thermal annealing.

Received 23rd November 2014,

Accepted 5th February 2015

DOI: 10.1039/c4nr06938b

www.rsc.org/nanoscale

### 1. Introduction

Co-assembly of polymers and inorganic components provides a powerful bottom-up approach to construct multi-functional hybrid materials with fancy properties.<sup>1–6</sup> Various hybrid co-assemblies were developed with controllable morphologies including spheres,<sup>7,8</sup> cylinders,<sup>9,10</sup> vesicles,<sup>11,12</sup> and other complex structures ranging from zero to three dimensions.<sup>13–15</sup> These assemblies have great potential application in many fields such as medical imaging, drug delivery, and catalysis as a result of the combination of the useful chemical and mechanical properties of the polymer and the unique chemical, electronic, magnetic, and optical properties of the inorganic component. Since the spatial distribution of the nanoparticles in hybrid materials is one of the critical factors determining the properties of the obtained hybrid structure,<sup>16–18</sup> many efforts have been made towards the preparation of hybrid co-assemblies with controllable location of the inorganic component in the polymer matrix.<sup>19–23</sup>

By varying precursor composition<sup>24–27</sup> or environmental parameters<sup>28,29</sup> in co-assembly, various inorganic components such as nanoparticles (NPs) and nanorods have been located selectively in different portions of the hybrid co-assemblies.<sup>30,31</sup> Taton and co-workers<sup>32</sup> incorporated oleic acid-coated magnetic NPs into the hydrophobic core of spherical micelles of poly(styrene)-*block*-poly(acrylic acid) (PS-*b*-PAA). Eisenberg and co-worker<sup>33</sup> demonstrated a general approach for controlled incorporation of metal NPs into the central portion of a vesicle wall, based on NPs coated with the same block-polymer as the vesicles. Through a similar approach, they also achieved the controlled location of NPs in the hydrophobic core of PS-*b*-PAA cylindrical micelles.<sup>34</sup> Park's group<sup>9,35</sup> achieved the dense packing of magnetic NPs in the walls of polymer vesicles and demonstrated that the spatial arrangement of NPs in the polymer matrix can affect the magnetic relaxation rate of the surrounding water. In these studies, the hydrophobic interaction, hydrogen bonding or electrostatic interactions, usually act as driving forces for co-assembly of inorganic NPs and polymers, and the distribution of NPs in the resulting hybrid co-assemblies is controlled by the thermodynamic equilibrium.<sup>23,36–38</sup> The arrangement of NPs in these researches is fixed during the process of co-assembly, and unchangeable after the formation of the hybrid co-assemblies, which means static control of the location of NPs. Another possible and feasible way to control the location of NPs is to change the morphology of the resulting hybrid co-assemblies

<sup>a</sup>School of Chemistry & Chemical Engineering, State Key Laboratory for Metal Matrix Composite Materials, Shanghai Jiao Tong University, 800 Dongchuan Rd., Shanghai 200240, China. E-mail: ponygle@sjtu.edu.cn

<sup>b</sup>School of Materials Science and Engineering, East China University of Science and Technology, 130 Meilong Rd., Shanghai 200237, China. E-mail: slin@ecust.edu.cn

†Electronic supplementary information (ESI) available: Experimental details; additional TEM images; DPD method. See DOI: 10.1039/c4nr06938b

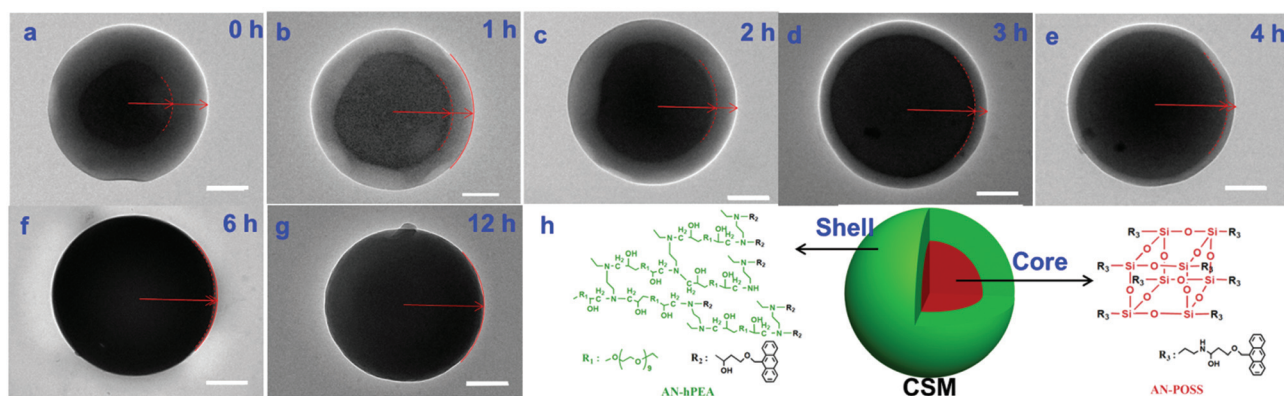


**Fig. 1** TEM tracing of CSM along thermal annealing at 85 °C for 0 (a), 1 (b), 2 (c), 3 (d), 4 (e), 6 (f), 12 (g) hour(s). Scale bar 200 nm. (h) Chemical structure of AN-hPEA and AN-POSS.

through post-treatment such as thermal or solvent annealing, which allows for tuning of the location of NPs.<sup>20,36</sup> To the best of our knowledge, however, the dynamic control of NPs' location in hybrid co-assemblies is rarely reported.

We herein demonstrate the first example of the dynamic control of the distribution of NPs in hybrid core-shell microspheres (CSM). The hybrid core-shell microspheres were prepared through co-assembly of amphiphilic hyperbranched poly(ether amine) (AN-hPEA) and polyhedral oligomeric silsesquioxanes (AN-POSS) NPs (Fig. 1h).<sup>39</sup> This core-shell structured morphology is thermodynamically metastable, and was captured by the crystallized aggregation of POSS in the core during the co-assembly of AN-POSS and AN-hPEA. Upon thermal annealing, diffusion of POSS from the core to the shell of AN-hPEA was observed, with this core-shell structure undergoing a transition to a thermodynamically more stable morphology with gradient distribution of POSS in the matrix of hPEA. During this process, the transitional state can be fixed by the cross-linking induced by photo-dimerization of anthracene,<sup>40</sup> and the spatial distribution of POSS can be controlled dynamically by the temperature and time of thermal annealing. Particular attention was paid to the effect of diffusion in the confined geometry on the spatial distribution of POSS in the hybrid microsphere.

## 2. Results and discussion

### 2.1 Morphology transition upon thermal annealing

A hybrid core-shell microsphere (CSM) was prepared through co-assembly of amphiphilic AN-hPEA and hydrophobic AN-POSS NPs. Previous work by our group<sup>39</sup> revealed that the resulting hybrid CSMs prefers a well-defined core-shell structure with low PDI of about 0.1, in which the core of the crystallized aggregation of AN-POSS is ~550 nm in diameter, and the hydrophilic shell of AN-hPEA is ~160 nm in thickness. In fact, the core-shell morphology of CSM is thermo-dynamically metastable, which is supported by differential scanning calorimetry (DSC) results (Fig. S1†). The DSC thermogram of the

obtained CSMs shows a microphase-separated structure. However, the composites of AN-hPEA/AN-POSS with various ratios prepared by mixing in solution exhibit only one glass transition in DSC thermograms and no phase separation was observed after several heat-cool loops, indicating that these composites of AN-hPEA/AN-POSS are homogenous, and that AN-hPEA & AN-POSS are completely compatible. In other words, AN-POSS can be dispersed in the polymer matrix of AN-hPEA on the molecular scale. The outstanding compatibility between AN-hPEA and AN-POSS might be ascribed to the strong  $\pi$ - $\pi$  interaction of anthracene moieties in AN-hPEA and AN-POSS. The DSC results revealed that the CSM is thermodynamically unstable and can transfer to a homogenous structure under certain conditions. Thus we make the assumption that, upon thermal annealing at a temperature higher than the melting point of AN-POSS, the microphase-separated core-shell structure may undergo spontaneously a transition to a more-stable homogeneous structure with a change of distribution of POSS NPs.

The uniform-sized and well-defined core-shell structure makes the hybrid microsphere an idea model to study the migration of NPs in confined geometry on the micro-scale. The morphology evolution of CSM on thermal annealing at 85 °C in water was recorded by TEM images and the migration of POSS from the core to the shell of AN-hPEA was observed. As shown in Fig. 1, the boundary between the core of AN-POSS (dark) and the shell of AN-hPEA can be observed before thermal annealing (0 h). During thermal annealing, the boundary shifts to the outside and the thickness of the shell becomes obviously thinner, indicating the migration of AN-POSS from the core to the shell of AN-hPEA.

At 85 °C, a temperature higher than the melting point of AN-POSS (~65 °C, Fig. 2a), the crystallization of AN-POSS in the core is destroyed and migration starts. During thermal annealing, AN-POSS in the core gradually migrates into the shell of AN-hPEA to form the transition layer, and the core of AN-POSS becomes smaller. The dark area in the CSM in TEM images (Fig. 1b-e) is comprised of the core of the crystallized AN-POSS and the transition layer composed of both AN-POSS

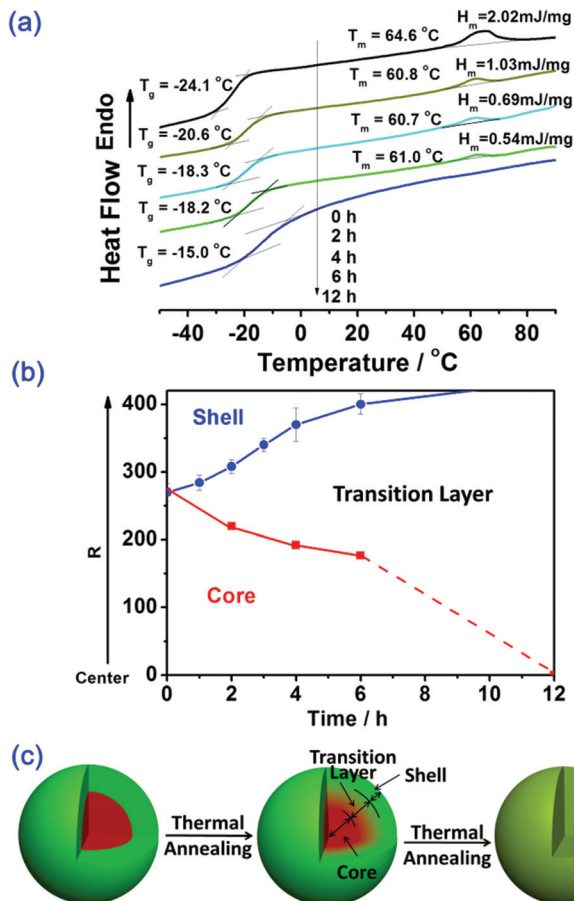


**Fig. 2** (a) DSC thermograms of CSM during thermal annealing at 85 °C for different times. (b) The dependence of the radius of the core ( $R_c$ ) and thickness of the transition layer ( $T_t$ ) and shell ( $T_s$ ) of CSM on thermal annealing at 85 °C. (c) The proposed scheme for the morphology transition of CSM during thermal-annealing.

and AN-hPEA. There is no obvious boundary between the core of POSS and the transition layer in the TEM images, which might be explained by the electron density of POSS being much higher than AN-hPEA. After annealing at 85 °C for 6 h, the shell of AN-hPEA almost disappeared, indicating that AN-POSS diffuses to the edge of CSM (Fig. 1f). Further thermal annealing leads the CSM to the more homogenous morphology (Fig. 1g). Although the interior morphology changes dramatically during thermal annealing, the shape and size of the hybrid co-assembly keeps almost unchanged, which is supported by SEM images and DLS results (Fig. S2†). This may be ascribed to the fact that the hydration shells of CSMs prevent them from fusing with each other. Moreover, cross-sectional TEM images of microspheres (Fig. S3†) were captured and the morphology transition from the microphase-separated core-shell to the homogeneous structure was further confirmed.

The morphology transition of the hybrid CSM during thermal annealing was also investigated by DSC. Fig. 2(a) shows DSC thermograms of CSM annealed for different lengths of time. Before thermal annealing, the CSM exhibits an obvious glass transition at -24.1 °C (the shell of AN-hPEA)

and a melting peak at around 65 °C (crystallized AN-POSS in the core). In comparison with the pure AN-POSS (Fig. S1†), the melting enthalpy ( $H_m$ ) of CSM (2.02 mJ mg<sup>-1</sup>) is around 1/3 of pure AN-POSS (6.20 mJ mg<sup>-1</sup>), which is almost the same as the feed ratio of AN-POSS in CSM. This result reveals that almost all AN-POSS in the feed prefers crystallized aggregation in the core of CSM. During thermal annealing at 85 °C, the glass transition temperature ( $T_g$ ) of the CSM increases, while the melting point ( $T_m$ ) and  $H_m$  shift slightly to the lower temperature and decreases obviously, respectively. The increased  $T_g$  of CSM might be ascribed to the migration of AN-POSS from the core to the shell of AN-hPEA. Generally, the incorporation of inorganic nanoparticles of POSS can enhance  $T_g$  of the soft polymer matrix.<sup>6</sup> Simultaneously, the size of the crystallized core of AN-POSS becomes smaller due to the diffusion of AN-POSS from the core to the shell of AN-hPEA, resulting in the decrease of  $H_m$ . This also means that the POSS core remains during thermal annealing. In other words, the extended dark core in the TEM images (Fig. 1b–d) should be comprised of the smaller core of the crystallized AN-POSS and the transition layer composed of AN-POSS and AN-hPEA.

After 6 hours of thermal annealing, the melting enthalpy ( $H_m$ ) of the CSM decreases to 0.54 mJ mg<sup>-1</sup> according to DSC (Fig. 2a), indicating that the crystallized core still exists although AN-POSS has diffused to the surface and the pure AN-hPEA shell disappears (Fig. 1e). After 6 hours of further thermal annealing (total 12 h), the melting peak disappears completely and only the glass transition at -12 °C can be observed in the DSC thermograms. The  $T_g$  of CSM after 12 h thermal annealing is close to that of AN-POSS-AN-hPEA = 1 : 2 composite (-9 °C, Fig. S1†), indicating that POSS NPs tend to disperse homogeneously in the hybrid CSMs after thermal annealing. The combination of TEM and DLS results can support the mechanism proposed in Fig. 2c, which illustrates the morphology transition of CSMs during thermal annealing: core-shell to core-transition-shell to homogeneous.

After revealing the interior morphology of CSMs during thermal annealing, it is necessary to determine quantitatively the size of the crystallized AN-POSS core ( $R_c$ , radius), the thickness of the transitional layer ( $T_t$ ) comprised of both AN-POSS and AN-hPEA, and the thickness of the AN-hPEA shell ( $T_s$ ). Since an obvious boundary between the transition layer and the shell can be observed in TEM images (Fig. 1),  $T_s$  was determined directly by TEM. The size of the crystallized AN-POSS core can be estimated from the  $H_m$  data shown in Fig. 2(a). Generally, the melting enthalpy can be used to estimate the amount of crystallized component, with the assumption that the materials keep a similar degree of crystallization after treatment. As  $H_m$  is proportional to the volume of the crystallized AN-POSS,  $R_{c(t)}$  can be given as follows:

$$R_{c(t)} = R_{c(0)} \times \left( \frac{H_m(t)}{H_m(0)} \right)^{1/3} \quad (1)$$

where  $R_{c(0)}$  and  $H_{m(0)}$  are the radius and melting enthalpy of the crystallized AN-POSS core before thermal annealing,

respectively. The thickness of the shell ( $T_s$ ) and the radius of the crystallized core ( $R_c$ ) dependent on thermal annealing time are presented in Fig. 2b. Based on the known  $T_s$  and  $R_c$ , and the almost unchanged size of the spheres of co-assembly (radius  $\sim 435$  nm, Fig. S2 $\dagger$ ), the thickness of the transitional layer ( $T_t$ ) can be calculated according to the formula:  $T_t = 435 \text{ nm} - R_c - T_s$ . Fig. 2(b) summarizes the obtained data regarding to  $R_c$ ,  $T_t$ , and  $T_s$  vs. time during thermal annealing. Upon thermal annealing, a transition layer is generated and its thickness ( $T_t$ ) increases with the time due to the diffusion of AN-POSS from core into the shell.

To understand fully the diffusion behaviour of AN-POSS in confined geometry, the thermal annealing of CSM at various temperatures was carried out. As the core-shell morphology is kinetically trapped by the crystallized aggregation of AN-POSS, this thermodynamically metastable state is expected to keep stable when the temperature is below the melting point of AN-POSS (65 °C). It is indeed true that CSM can retain the microphase-separated core-shell morphology for at least one month at room temperature. Even after heating at 55 °C for 48 h, no obvious change was found in the size of the crystallized core and the shell of CSM (Fig. 3c), which is in contrast to the obvious morphology transition at 85 °C. This can be explained by the fact that crystallization restricts the mobility of AN-POSS, resulting in no diffusion of AN-POSS from the core to the shell of AN-hPEA. When the annealing temperature is higher than  $T_m$  (65 °C and 75 °C), CSM takes a similar morphology transition to that annealed at 85 °C, and the dark area of CSM in the TEM images expands with the increase of annealing time (Fig. 3a and b). The speed of the dark core increase is obviously slower at lower temperature. The shell of AN-hPEA disappeared after being heated at 75 °C for 48 h, while the shell with a thickness of 75 nm can still be seen in the TEM images even after thermal annealing at 65 °C for 48 h. The temperature dependence of the CSM morphologic transition confirms that the migration of AN-POSS into the shell of AN-hPEA is controlled by diffusion. A higher tempera-

ture can provide higher molecular mobility, resulting in faster diffusion of AN-POSS into the shell of AN-hPEA, and consequently quicker morphology transition.

## 2.2 Dissipative particle dynamics (DPD) simulations

The above results reveal that the morphologies of the hybrid microspheres change with the diffusion of AN-POSS in a confined geometry during the annealing process. To give a clear view of the motion of the nanoparticles, dissipative particle dynamics (DPD) simulations<sup>41,42</sup> were performed to investigate the structural evolution of CSM during thermal annealing. A core-shell structured model before thermal-annealing (0 time-steps) was constructed (Fig. 4, Scheme S1g $\dagger$ ), where AN-hPEA and AN-POSS were represented by green and red beads, respectively. The simulation details can be found in the ESI $\dagger$ .

Fig. 4 presents clearly the sectional views of five typical stages of simulated CSM morphologies during the thermal annealing process. During thermal annealing, AN-POSS nanoparticles (red beads) in the core diffuse gradually into the shell of AN-hPEA (green beads), leading to the appearance of a transitional layer containing both AN-hPEA and AN-POSS. The thickness of the transitional layer is about 1/4 of the radius of CSM at  $2.4 \times 10^4$  timesteps (corresponding to 2 h annealing). The shell thickness decreases further as the annealing time increases while the thickness of the transitional layer increases. The shell of AN-hPEA almost disappears at  $7.2 \times 10^4$  timesteps (corresponding for 6 h annealing). When the annealing time is  $2.88 \times 10^5$  timesteps (corresponding to 24 h annealing), the CSM exhibits a near homogenous structure with AN-hPEA and AN-POSS mixed freely. The simulation results reproduce the general features of the morphological transition of CSM upon thermal annealing. In addition, the simulations provide information on the spatial distribution of AN-POSS in CSM, capturing more microscopic details of the CSM structure. Fig. 4b shows the normalized density profiles of AN-POSS along the radius direction at various annealing times. The DPD results reflect some characteristics of diffusion-controlled

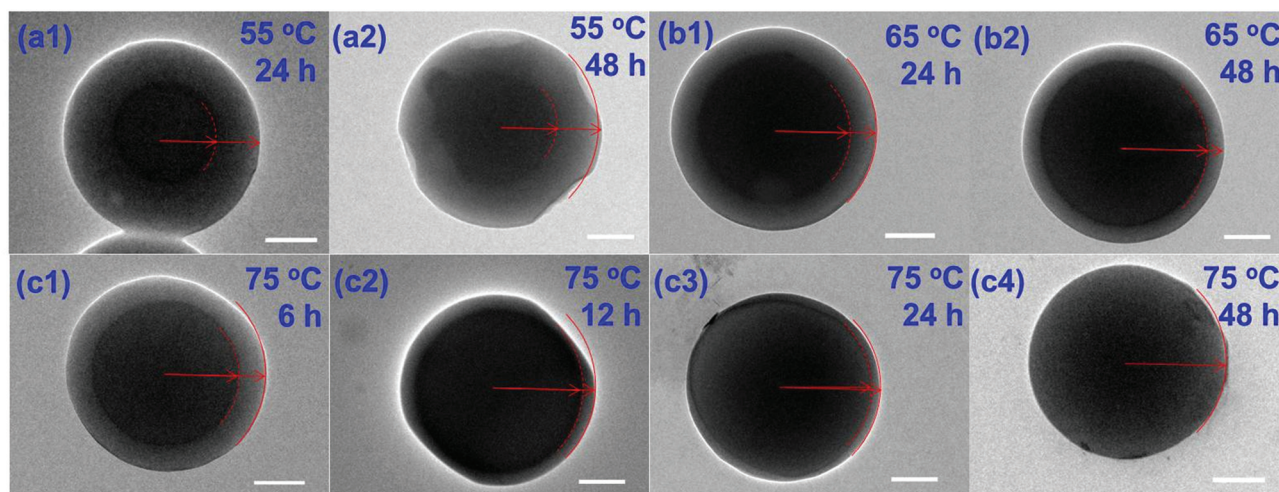


Fig. 3 TEM images of CSM along thermal annealing at different temperatures (a) 55 °C; (b) 65 °C; (c) 75 °C. Scale bar 200 nm.

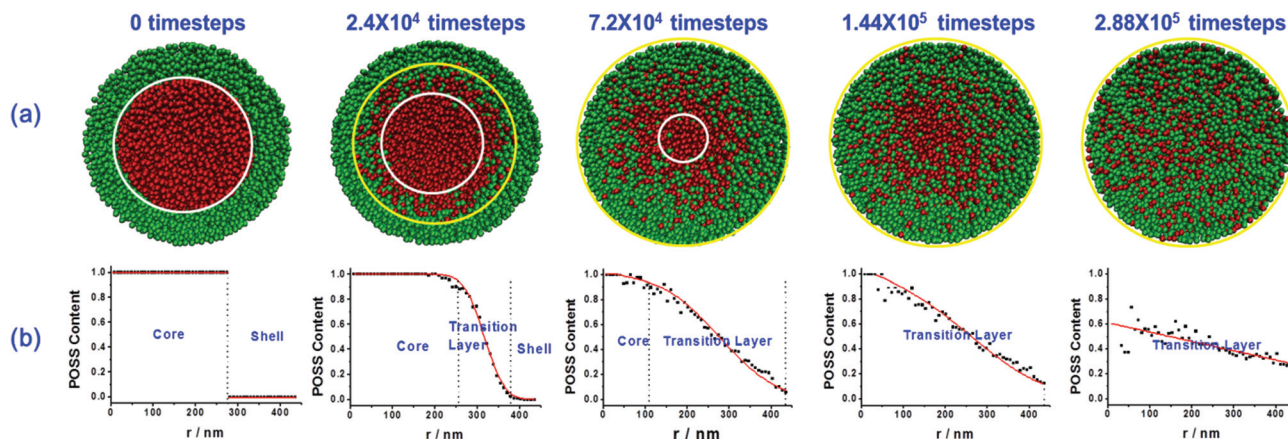


Fig. 4 Simulated snapshots of CSM (section of the center) at various annealing times according DPD simulations, which show the morphology transition from a core-shell structure to a core-transition-shell structure and to a homogeneous structure. The green and red beads refer to AN-hPEA and AN-POSS, respectively. Corresponding spatial distribution of AN-POSS in CSM along the radius direction at different annealing timesteps are shown in Fig. S4.† Note:  $1.2 \times 10^5$  timesteps correspond to 1 hour of thermal annealing.

behaviour, and supported the proposed mechanism of structural evolution of CSM (Fig. 2c).

### 2.3 Dynamical control of NPs' location in hybrid CSM

Spatial distribution in composition is of considerable interest in the design of new materials: programmable materials, optical materials, and damping materials *etc.*<sup>43–45</sup> For example, because the continuously changing composition can minimize reflection at the interface of two materials, this can increase optical transmittance and enhancing the resolution of optical materials.

Thus, the control of the spatial distribution of nanoparticles in hybrid assemblies is necessary. As the spatial distribution of POSS in CSM on thermal annealing shows some characteristics of diffusion, Fick's second law of diffusion<sup>46,47</sup> (eqn (2)) is used to predict the migration of AN-POSS from the core to shell of CSM.

$$\frac{\partial C}{\partial t} = D \frac{\partial^2 C}{\partial r^2} \quad (2)$$

where  $D$ ,  $C$ ,  $t$  and  $r$  are the diffusion constant, concentration, time and radial axis, respectively. Eqn (2) can be expressed as follows:<sup>46</sup>

$$C(r) = \frac{C_0}{2} \left\{ \operatorname{erf} \left[ \frac{(r_0 - r)}{2\sqrt{Dt}} \right] + \operatorname{erf} \left[ \frac{(r_0 + r)}{2\sqrt{Dt}} \right] \right\} - \frac{\sqrt{Dt}}{\pi} \left\{ \exp \left[ \frac{-(r_0 - r)^2}{4Dt} \right] - \exp \left[ \frac{-(r_0 + r)^2}{4Dt} \right] \right\} \quad (3)$$

Eqn (3) gives the concentration of AN-POSS along the radial axis at different times of thermal annealing.  $C_0$  is the concentration in the core of the crystallized AN-POSS aggregate and can be regarded as 1.0 (100%).  $r_0$  is the radius of the core, 275 nm. Based on the shell thickness of a hybrid microsphere at different times of thermal annealing, determined by TEM, the diffusion constant ( $D$ ) of AN-POSS in the shell of AN-hPEA

at different temperatures can be calculated according to eqn (3). The diffusion constant ( $D$ ) of AN-POSS at 85, 75, and 65 °C is 0.120, 0.038, and 0.009 nm<sup>2</sup> S<sup>-1</sup>, respectively. The diffusion constant is very low, and increases almost 13 times when the temperature is increased from 65 to 85 °C. This low diffusion constant might be ascribed to the hydrodynamic volume of AN-POSS, which is much bigger than the low-molecular-weight molecules, resulting in lesser mobility and slower diffusion in the polymer matrix.

Fig. S5† shows the linear Arrhenius plot, from which the diffusion activation energy ( $Q$ ) is calculated to be 130.4 kJ mol<sup>-1</sup>. The high diffusion activation energy might be also ascribed to the nature of AN-POSS as NPs. The spatial distribution of AN-POSS along the thermal annealing at 85 °C is further calculated according to eqn (3) and shown in Fig. 5, which reveals the detailed changes in AN-POSS concentration

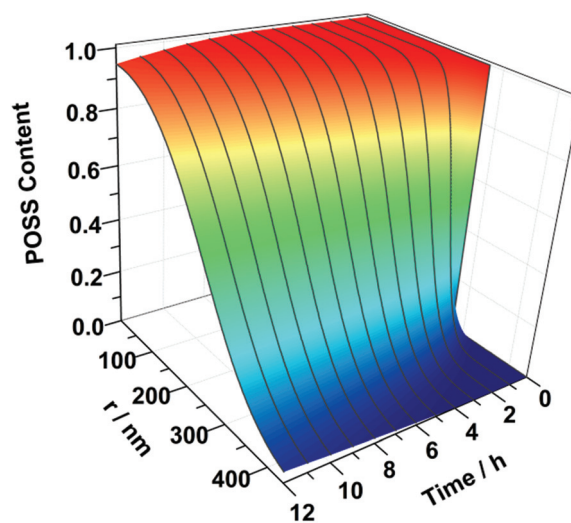


Fig. 5 The spatial distribution of AN-POSS in hybrid microsphere along the radius at different annealing times, which is calculated from the Fick's second law (annealing temperature is 85 °C).

along the axis with the time of thermal annealing. To simplify eqn (3), the concentration of AN-POSS in the core and the shell is defined as 1.0 and 0, respectively. Due to the difference of concentration between the core and shell, AN-POSS diffuses into the hPEA shell along the axis during thermal annealing. The spatial distribution of AN-POSS changes quickly at the beginning of thermal annealing, and becomes slower in the later stages. This is typical diffusion behaviour driven by concentration difference. Before thermal annealing, the concentration of AN-POSS at the interface between the core and shell shows a sharp change from 1 to 0. During thermal annealing, the transition layer is generated and expands into the whole CSM, in which the concentration of AN-POSS decreases gradually along the axis. Further thermal annealing makes the concentration difference along the axis smaller, leading to a more homogeneous morphology. Fig. 5 predicts the concentration gradient of AN-POSS along the axis in the transitional layer at different times of thermal annealing, which cannot be determined by TEM images of the hybrid microsphere. The concentration gradient along the axis decreases with the increase of thermal time. As shown in Fig. 5, the core of the crystallized AN-POSS disappears after thermal annealing for 10 h, which is in agreement with the DSC results.

To verify the feasibility of this strategy for the dynamical control of NPs' location, another core-shell hybrid co-assembly of AN-POSS/AN-hPEA = 1/1 was also annealed thermally at 85 °C (Fig. 6). They undergo the same morphology transition from the core-shell to core-transition-shell to homogeneous structure (Fig. 6). Eqn (3) was utilized to predict the distribution of AN-POSS NPs in CSM-2. Substituting the variables ( $D = 0.120 \text{ nm}^2 \text{ s}^{-1}$ ;  $r_0 = 351 \text{ nm}$ ;  $r = 1, 2, \dots, 466$ ) into the eqn (3), gives the distribution AN-POSS NPs in CSM-2. Both predicted shell thickness and experimental data were summarized in Table 1. The predicted data meet with experimental data well,

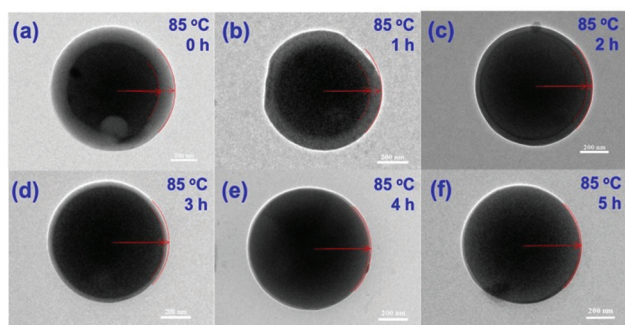


Fig. 6 TEM images of CSM-2 (AN-hPEA/AN-POSS = 1/1) upon different annealing times (85 °C). Scale bar 200 nm.

Table 1 Shell thickness ( $T_s$ ) of CSM-2 upon different annealing time (85 °C)

Annealing time/h	0	1	2	3	4	5
Predicted/nm		69	51	38	27	18
Experimental/nm	115	78	50	38	17	10

indicating the feasibility of controlling the distribution of NPs in CSMs.

Furthermore, the transition state of CSM can be fixed by the cross-linking-induced by photo-dimerization of anthracene.<sup>40</sup> After exposure to 365 nm UV-light for 15 min the dimerization degree of AN groups is around 75% (Fig. S5a, b†). The morphology is retained well in tetrahydrofuran (THF) solution, suggesting that the whole microsphere is tightly cross-linked (Fig. S6c†). Even under further thermal annealing at 85 °C, the cross-linked temporary morphology does not exhibit any obvious change (Fig. S5d and e†). This can be explained by that the cross-linking *via* dimerization of AN moieties freezes the mobility of AN-POSS and AN-hPEA, leading to no diffusion of AN-POSS from the core to the shell. Therefore, combination of thermal annealing and photo-cross-linking provides an approach to dynamic control of the spatial distribution of AN-POSS in these hybrid co-assemblies.

#### 2.4 Mechanical performance of hybrid gradient microsphere

AFM is powerful to detect the mechanical properties of materials with nano-scale, and provide some insights into the fine details of polymer surfaces and interfaces.<sup>48–50</sup> Force curve measurements are carried out by AFM to assess the mechanical properties of the annealed hybrid microsphere: the sample is compressed by the indenting AFM tip and the elastic response of the sample under this loading force is analyzed. Young's modulus ( $E$ ) is calculated from the force curves using the Hertz model. To enhance the stability, the annealed hybrid microsphere is cross-linked by irradiation of 365 nm UV-light before AFM measurement.

Fig. 7a shows the representative force curves during thermal annealing at 85 °C. Since the diameter of the hybrid microsphere in this study is over 800 nm, the fitting analysis range is  $z = 0–60 \text{ nm}$  (*i.e.*, less than 10% of the CSM height) of the force curves to determine  $E$  values. Fig. 7b presents  $E$  values at various annealing times which are calculated by averaging multiple probing points. The Young's modulus is 12 MPa before thermal annealing and remains almost unchanged during thermal annealing for the first 3 h, which is comparable to the 13 MPa of the pure AN-hPEA matrix (Fig. S7†). This confirms that the hybrid microsphere is covered by a thick shell of AN-hPEA even after thermal annealing for 3 h, which is in good agreement with the results of TEM. After annealing for 4 h, the Young's modulus increases to 75 MPa although the hybrid microsphere at this stage still keeps the core-transition layer-shell structure. This might be explained by that the transitional layer can act as a substrate to influence the  $E$  value.<sup>51</sup> In other words, the  $E$  value of 75 MPa is determined by AFM results from both the shell and transitional layer. Generally, the incorporation of POSS nanoparticles can enhance the mechanical properties of the polymer matrix such as modulus and hardness. The enhanced  $E$  value of CSM should be ascribed to the increasing concentration of AN-POSS near to the surface of the hybrid microsphere, resulting from the diffusion of AN-POSS from the center to the surface. After annealing for 12 h, the Young's modulus increases to 310

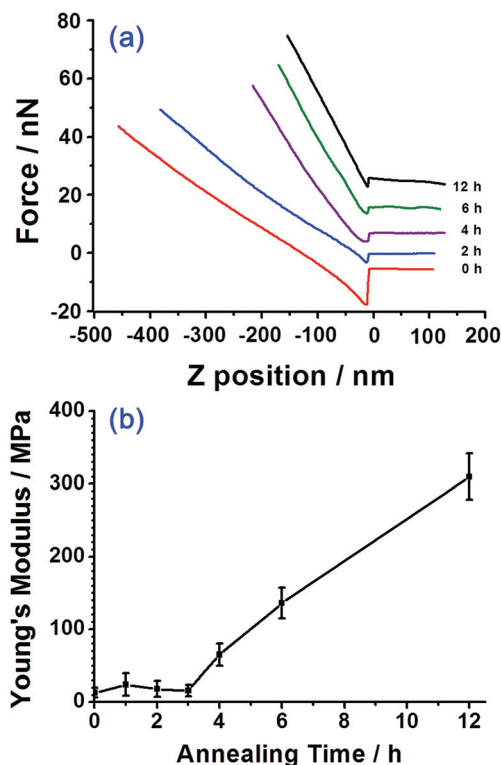


Fig. 7 Typical force curves (a) and the Young's modulus (b) of hybrid microspheres annealed at 85 °C for different times.

MPa, on the same order of magnitude to that of the AN-POSS/AN-hPEA composite (Fig. S6,† POSS content 0.33, 410 MPa). This indicates that the concentration of AN-POSS near the surface of CSM increases and the distribution of AN-POSS in the hybrid microsphere becomes more homogeneous during thermal annealing. These results of the measurement of AFM force curves can be well explained by the morphology transition, which were revealed by both experimental results of TEM and theoretical study.

### 3. Experimental

#### 3.1 Preparation of core-shell microspheres (CSM) and their thermal annealing

The preparation of core-shell microspheres was discussed in detail in our previous work.<sup>39</sup> Typically, 6.6 mg of AN-hPEA and 3.3 mg of AN-POSS were first dissolved into 1 mL of dioxane, which is a good solvent for both AN-hPEA and AN-POSS. The solution was equilibrated at 25 °C for 1 hour before 9 mL of milli-Q water was added slowly to the solution (5 mL of water per hour). The polymer solution was gently stirred during the water addition process. Then, the samples were dialyzed against water for 24 h and collected for further treatment. The CSM described in this paper is not cross-linked unless specifically noted.

In a typical annealing process, 10 ml of CSM aqueous solution (1 mg ml<sup>-1</sup>) was added to a 25 ml bottle. Then the CSM

aqueous solution was placed in a precisely controlled heater (IKA RET Basic equipped with ETS-D5, Germany) under gentle stirring.

### 4. Conclusion

In summary, the spatial distribution of POSS in the hybrid microsphere can be predicted and controlled dynamically through a diffusion approach. The hybrid core-shell microsphere (CSM) prepared by co-assembly of AN-POSS and AN-hPEA was taken as a model, in which the shell is comprised of AN-hPEA and the core is comprised of the crystallized aggregation of AN-POSS. Upon thermal annealing at a temperature higher than the melting point of AN-POSS, the diffusion of AN-POSS from the core to shell of CSM leads to a transition of morphology from the core-shell structure to core-transition-shell to the thermodynamically more stable homogeneous morphology, which was confirmed by the experimental results of TEM and DSC, theory calculations of Fick's second law of diffusion and DPD simulation. During this process, the location of POSS in CSM can be controlled dynamically by the temperature and time of thermal annealing. AFM force curves revealed that the spatial distribution of POSS nanoparticles generates a significant influence on the mechanical properties of CSM. Generally, for a phase-separated system with two compatible components, this process can be used to fabricate hybrid materials with controlled location of nanoparticles in micro-assemblies including core-shell spheres and other heterogeneous structures trapped by kinetics. We believe that this concept for the dynamical control of nanoparticle location by diffusion can provide new guidelines for the design and preparation of hybrid co-assemblies with desired functions and properties.

### Acknowledgements

The authors thank the National Nature Science Foundation of China (21174085, 21274088, 51103044) for their financial support. We also thank Prof. Z. H. Luo for his helpful discussion on the diffusion equation. X. Jiang and S. Lin are supported by the NCET-12-3050 and NCET-12-0857 Projects, respectively.

### Notes and references

- 1 A. C. Balazs, T. Emrick and T. P. Russell, *Science*, 2006, **314**, 1107–1110.
- 2 A. H. Lu, E. L. Salabas and F. Schuth, *Angew. Chem., Int. Ed.*, 2007, **46**, 1222–1244.
- 3 M. C. Daniel and D. Astruc, *Chem. Rev.*, 2004, **104**, 293–346.
- 4 M. C. Orilall and U. Wiesner, *Chem. Soc. Rev.*, 2011, **40**, 520–535.
- 5 Z. Nie, A. Petukhova and E. Kumacheva, *Nat. Nanotechnol.*, 2010, **5**, 15–25.

- 6 W. A. Zhang and A. H. E. Muller, *Prog. Polym. Sci.*, 2013, **38**, 1121–1162.
- 7 B. Yan, J.-C. Boyer, N. R. Branda and Y. Zhao, *J. Am. Chem. Soc.*, 2011, **133**, 19714–19717.
- 8 J.-F. Berret, N. Schonbeck, F. Gazeau, D. El Kharrat, O. Sandre, A. Vacher and M. Airiau, *J. Am. Chem. Soc.*, 2006, **128**, 1755–1761.
- 9 Q. Luo, R. J. Hickey and S.-J. Park, *ACS Macro Lett.*, 2013, **2**, 107–111.
- 10 J. Y. Yuan and A. H. E. Muller, *Polymer*, 2010, **51**, 4015–4036.
- 11 C. Sanson, O. Diou, J. Thévenot, E. Ibarboure, A. Soum, A. Brûlet, S. Miraux, E. Thiaudière, S. Tan, A. Brisson, V. Dupuis, O. Sandre and S. Lecommandoux, *ACS Nano*, 2011, **5**, 1122–1140.
- 12 M. R. Rasch, E. Rossinyol, J. L. Hueso, B. W. Goodfellow, J. Arbiol and B. A. Korgel, *Nano Lett.*, 2010, **10**, 3733–3739.
- 13 Y. Guo, S. Harirchian-Saei, C. M. S. Izumi and M. G. Moffitt, *ACS Nano*, 2011, **5**, 3309–3318.
- 14 M. S. Nikolic, C. Olsson, A. Salcher, A. Kornowski, A. Rank, R. Schubert, A. Frömsdorf, H. Weller and S. Förster, *Angew. Chem., Int. Ed.*, 2009, **48**, 2752–2754.
- 15 M. R. Bockstaller, R. A. Mickiewicz and E. L. Thomas, *Adv. Mater.*, 2005, **17**, 1331–1349.
- 16 E. González, J. Arbiol and V. F. Puntes, *Science*, 2011, **334**, 1377–1380.
- 17 Y. Yin and A. P. Alivisatos, *Nature*, 2005, **437**, 664–670.
- 18 S. Liu, Z. Sun, Q. Liu, L. Wu, Y. Huang, T. Yao, J. Zhang, T. Hu, M. Ge, F. Hu, Z. Xie, G. Pan and S. Wei, *ACS Nano*, 2014, **8**, 1886–1892.
- 19 Y. Mai and A. Eisenberg, *Acc. Chem. Res.*, 2012, **45**, 1657–1666.
- 20 S. G. Jang, D. J. Audus, D. Klinger, D. V. Krogstad, B. J. Kim, A. Cameron, S.-W. Kim, K. T. Delaney, S.-M. Hur, K. L. Killips, G. H. Fredrickson, E. J. Kramer and C. J. Hawker, *J. Am. Chem. Soc.*, 2013, **135**, 6649–6657.
- 21 T. Chen, M. Yang, X. Wang, L.H. Tan and H. Chen, *J. Am. Chem. Soc.*, 2008, **130**, 11858–11859.
- 22 B. L. Sanchez-Gaytan, W. Cui, Y. Kim, M. A. Mendez-Polanco, T. V. Duncan, M. Fryd, B. B. Wayland and S.-J. Park, *Angew. Chem., Int. Ed.*, 2007, **46**, 9235–9238.
- 23 W. Li, S. Liu, R. Deng and J. Zhu, *Angew. Chem., Int. Ed.*, 2011, **50**, 5865–5868.
- 24 R. J. Hickey, J. Koski, X. Meng, R. A. Riggleman, P. Zhang and S.-J. Park, *ACS Nano*, 2014, **8**, 495–502.
- 25 J. J. Chiu, B. J. Kim, E. J. Kramer and D. J. Pine, *J. Am. Chem. Soc.*, 2005, **127**, 5036–5037.
- 26 L. H. Tan, H. Xing, H. Chen and Y. Lu, *J. Am. Chem. Soc.*, 2013, **135**, 17675–17678.
- 27 L. Zhang, J. Lin and S. Lin, *Macromolecules*, 2007, **40**, 5582–5592.
- 28 X. Yu, S. Zhong, X. Li, Y. Tu, S. Yang, R. M. Van Horn, C. Ni, D. J. Pochan, R. P. Quirk, C. Wesdemiotis, W.-B. Zhang and S. Z. D. Cheng, *J. Am. Chem. Soc.*, 2010, **132**, 16741–16744.
- 29 S. G. Jang, B. J. Kim, C. J. Hawker and E. J. Kramer, *Macromolecules*, 2011, **44**, 9366–9373.
- 30 A. Walther and A. H. E. Müller, *Chem. Rev.*, 2013, **113**, 5194–5261.
- 31 A. H. Groschel, A. Walther, T. I. Lobling, F. H. Schacher, H. Schmalz and A. H. E. Muller, *Nature*, 2013, **503**, 247–251.
- 32 B.-S. Kim, J.-M. Qiu, J.-P. Wang and T. A. Taton, *Nano Lett.*, 2005, **5**, 1987–1991.
- 33 Y. Mai and A. Eisenberg, *J. Am. Chem. Soc.*, 2010, **132**, 10078–10084.
- 34 Y. Mai and A. Eisenberg, *Macromolecules*, 2011, **44**, 3179–3183.
- 35 R. J. Hickey, A. S. Haynes, J. M. Kikkawa and S.-J. Park, *J. Am. Chem. Soc.*, 2011, **133**, 1517–1525.
- 36 S. G. Jang, A. Khan, C. J. Hawker and E. J. Kramer, *Macromolecules*, 2012, **45**, 1553–1561.
- 37 R. J. Hickey, Q. Luo and S.-J. Park, *ACS Macro Lett.*, 2013, **2**, 805–808.
- 38 S. Yang, C.-F. Wang and S. Chen, *J. Am. Chem. Soc.*, 2011, **133**, 8412–8415.
- 39 Z. Su, B. Yu, X. Jiang and J. Yin, *Macromolecules*, 2013, **46**, 3519–3528.
- 40 B. Yu, X. S. Jiang and J. Yin, *Soft Matter*, 2011, **7**, 6853–6862.
- 41 Y.-J. Sheng, C.-H. Nung and H.-K. Tsao, *J. Phys. Chem. B*, 2006, **110**, 21643–21650.
- 42 Y. Xu, J. Feng, H. Liu and Y. Hu, *Mol. Simul.*, 2008, **34**, 559–565.
- 43 Y. Liu, M. Takafuji, H. Ihara, M. Zhu, M. Yang, K. Gu and W. Guo, *Soft Matter*, 2012, **8**, 3295–3299.
- 44 N. Zhao, Z. Wang, C. Cai, H. Shen, F. Liang, D. Wang, C. Wang, T. Zhu, J. Guo, Y. Wang, X. Liu, C. Duan, H. Wang, Y. Mao, X. Jia, H. Dong, X. Zhang and J. Xu, *Adv. Mater.*, 2014, **26**, 6994–7017.
- 45 T. Konig, P. Ledin, M. Russell, J. Geldmeyer, M. Mahmoud, M. A. El-Sayed and V. V. Tsukruk, *Nanoscale*, 2015, DOI: 10.1039/C4NR06430E.
- 46 J. Crank, *The Mathematics of Diffusion*, Oxford University Press, 1979.
- 47 F. D. Fischer and J. Svoboda, *Prog. Mater. Sci.*, 2014, **60**, 338–367.
- 48 M. E. McConney, S. Singamaneni and V. V. Tsukruk, *Polym. Rev.*, 2010, **50**, 235–286.
- 49 H. Y. Yoshikawa, F. F. Rossetti, S. Kaufmann, T. Kaindl, J. Madsen, U. Engel, A. L. Lewis, S. P. Armes and M. Tanaka, *J. Am. Chem. Soc.*, 2011, **133**, 1367–1374.
- 50 H. Liu, N. Chen, S. Fujinami, D. Louzguine-Luzgin, K. Nakajima and T. Nishi, *Macromolecules*, 2012, **45**, 8770–8779.
- 51 J. Domke and M. Radmacher, *Langmuir*, 1998, **14**, 3320–3325.